Separation and Purification Technology 277 (2021) 119483

Contents lists available at ScienceDirect

Separation and Purification Technology

journal homepage: www.elsevier.com/locate/seppur

Microchannel zeolite 13X adsorbent with high CO_2 separation performance

Jonas Hedlund [a], Gustavo Garcia [a], Marco Balsamo [b], Ming Zhou [a,*], Johanne Mouzon [a]

[a] Chemical Technology, Luleå University of Technology, SE-971 87 Luleå, Sweden
[b] Dipartimento di Scienze Chimiche, Università degli Studi di Napoli Federico II, Complesso Universitario di Monte Sant' Angelo, 80126 Napoli, Italy

ARTICLE INFO

Keywords:
Adsorption
Phase separation
Oriented monolayer
Monolithic adsorbents
13X zeolite
CO_2 capture

ABSTRACT

Uniform 13X films with thicknesses of 3 and 11 μm were grown on supports in the form of steel monoliths with a cell density of 1600 cpsi and microchannels width of 0.5 mm. Sharp breakthrough fronts and a dynamic uptake of 3.4 mmol CO_2 g^{-1} zeolite were observed in the forwarding step of breakthrough experiments for a feed of 10% CO_2 in N_2 with a high flow rate at 293 K and 1 bar. Numerical modeling showed that the adsorption process was very fast and that the transport of CO_2 in the thin zeolite layer was the rate-limiting step, the mass transfer resistance for the 11 μm film is 2.2 times lower than zeolite 13X pellets and 100 times lower than zeolite 4A beads. Axial dispersion, pressure drop, and gas film resistance were shown to be negligible. The steel monolith support provides good mechanical strength and excellent thermal conductivity for the 13X films. The combination of properties makes this adsorbent a good performer when compared with other types of structured zeolite adsorbents in reported literatures. This microchannel adsorbent is a promising alternative to traditional adsorbents in processes of fast CO_2 separation with short cycle times.

1. Introduction

Current industrial CO_2 separation methods are based on aqueous amines [1], membranes [2–4], and adsorbents [5–7]. Amine scrubbing is frequently used in industry, but has some drawbacks such as very energy consuming regeneration, amine degradation and corrosion [8]. Another industrial method for CO_2 separation is polymeric membranes, which separates CO_2 selectively via several different mechanisms, but an ideal membrane with high stability, selectivity, flux and reproducibility is not yet industrially available [9]. Packed beds of adsorbent pellets are mostly used in adsorption processes. The main disadvantages with pelletized adsorbents are that the material may erode due to thermal cycling and mechanical vibration, which generate fine particles that may leave the adsorption column. Besides, packed beds of pellets display a large pressure drop which is problematic at short cycle times [10]. Furthermore, the slow mass transfer kinetics at both the film- and molecular-levels as big of an issue as the pressure drop.

Considerable interest has been shown in the area of process intensification [11], and the application of a monolithic absorbent can be one of the means towards achieving it. The technique of 3D printing promotes the preparation of porous adsorbents and the chemical, structural, as well as mechanical properties of the adsorbent material can be optimised for gas separation processes [12]. As an example, 3D printed zeolite 13X monoliths were reported to exhibit good mechanical properties and a high dynamic CO_2 adsorption capability of 3.97 mmol g^{-1} for a 15/85 CO_2/N_2 mixture [13]. The main disadvantages of 3D printing are slow manufacturing output compared to pelletization and extrusion and slow mass transfer properties, which may result in high costs of the adsorbent material and difficulties to scale-up [14–16].

Adsorbents in monolith-shape with parallel channels have potential for real applications because of the excellent geometry, which bring about low pressure drop, uniform flow pattern and lower attrition [17–19]. Good mass transfer can be achieved for thin films of adsorbent material grown on monolithic supports, due to the short diffusion path in a thin film [20].

Faujasite (FAU) type zeolite has a cubic unit cell and a framework comprising so-called 12-ring pores running in the (111) directions of the crystals. The pore size of the ring is about 7.4 Å, but the effective pore diameter is dependent on the type of counter ions in the zeolite. Both X and Y type of zeolites have FAU framework, and the molar ratio of Si/Al is per definition between 1 and 1.5 for X type and higher than 1.5 for zeolite Y [21]. The sodium form of X type is indicated as zeolite 13X. It readily adsorbs CO_2 and Rodrigues et al. reported an adsorption capacity of 2.5 mol CO_2/kg zeolite [22]. Myers et al. reported capacity of 3.6 mol CO_2/kg zeolite at 31.4 °C for zeolite 13X powder [23]. However, Kroll et al. reported an even higher CO_2 capacity of 5 mol/kg at 30 °C and 1 bar [24]. Furthermore, this zeolite displays a high CO_2/N_2 adsorption

* Corresponding author.
E-mail addresses: jonas.hedlund@ltu.se (J. Hedlund), ming.zhou@ltu.se (M. Zhou).

https://doi.org/10.1016/j.seppur.2021.119483
Received 18 May 2021; Received in revised form 11 August 2021; Accepted 11 August 2021
Available online 17 August 2021

Nomenclature

C	CO_2 concentration in the gas phase [mol m^{-3}]
C_0	CO_2 concentration in the gas phase at the adsorber inlet [mol m^{-3}]
C_{out}	CO_2 concentration in the gas phase at the adsorber outlet [mol m^{-3}]
d_h	hydraulic diameter [m]
D_{ax}	axial dispersion coefficient [m^2 s^{-1}]
$D_{CO_2\text{-}N_2}$	CO_2 molecular diffusivity in the gas phase [m^2 s^{-1}]
D_z	zeolite film diffusivity [m^2 s^{-1}]
F	Flow rate of during breakthrough experiment [m^3 s^{-1}]
k_{ext}	fluid film mass transfer coefficient [m s^{-1}]
k_{ov}	overall mass transfer coefficient [s^{-1}]
K_H	Henry equilibrium constant [mol kg^{-1} bar^{-1}]
L	total length of the honeycomb adsorbent [m]
m	mass of zeolite [kg]
P	pressure [bar]
P*	CO_2 equilibrium partial pressure in the gas phase [bar]
p_{CO_2}	partial pressure of CO_2 in the feed gas [Pa]
q	adsorption capacity of zeolite [mol kg^{-1}] estimated from time to reach $C/C_0 = 0.5$
q^{model}	adsorption capacity of zeolite [mol kg^{-1}] estimated from the fitted model
R	ideal gas constant [J mol^{-1} K^{-1}]
Re	Reynolds number [−]
R_{ext}	fluid film diffusion resistance [s]
R_{ov}	overall mass transfer resistance [s]
R_z	zeolite film diffusion resistance [s]
Sc	Schmidt number [−]
Sh	Sherwood number [−]
t	time [s]
T	temperature [K]
u	gas velocity in the monolith channel [m s^{-1}]
x_z	mass fraction of zeolite in the structured adsorbent [kg kg^{-1}]
z	adsorbent bed axial coordinate [m]

Greek symbols

δ	zeolite film thickness [m]
ΔP	pressure drop [bar]
ε	monolith void fraction [−]
μ	gas dynamic viscosity [kg m^{-1} s^{-1}]
ρ_g	gas density [kg m^{-3}]
ρ_b	adsorbent bulk density [kg m^{-3}]
$\overline{\omega}$	average adsorption capacity of the structured adsorbent [mol kg^{-1}]
ω*	equilibrium adsorption capacity of the structured adsorbent [mol kg^{-1}]

selectivity of about 500 at 298 K and 1 bar [25]. Ho et al. have shown that a good adsorbent with CO_2 selectivity of 500 is enough to lower the cost of CO_2 capture substantially for flue gas from a power plant. Adsorbents with even higher selectivity has little effect on the cost reduction of CO_2 capture [26]. The adsorption selectivity of zeolite 13X is a result of polarizability and larger quadrupole moment of CO_2 (14.3×10^{-40} C m^2) compared to N_2 (4.7×10^{-40} C m^2) [7]. A 13X adsorbent is stable and can be used for hundreds of adsorption–desorption cycles, which makes it a cost-effective adsorbent [10]. A limitation of zeolite 13X is the competitive adsorption of water, leading to reduced selectivity for CO_2 in humid flue gases [27]. However, this drawback can be remedied by chemical grafting of amine via formation of a conjugated acid–base between the zeolite Brønsted acid site and e.g., ethylenediamine [28].

We have previously explored parallel channel cordierite monoliths coated with thin zeolite 13 X films for carbon dioxide separation. The monoliths showed remarkable sharper breakthrough fronts and the pressure drop was notably lower than zeolite pellets [29–31]. A model revealed that in short cycle times, the monolithic adsorbent could even achieve better productivity than beads or pellets although the single time capacity was lower [30]. It was also illustrated by numerical modelling and experiments that the cordierite monoliths have highly porous walls, which had a negative influence on the breakthrough front. The pores in the cordierite walls bring about pore filling with CO_2 and N_2 gas mixture, not selective CO_2 adsorption [31]. Also, to achieve sufficient adsorption capacity, the film thickness should be sufficiently large without compromising the kinetics. It was shown that a film thickness of 20 or 30 μm resulted in broadening of the CO_2 breakthrough front, due to increased mass transfer resistance, but films with a thickness of about 10 μm thickness displayed sharp fronts [31]. Consequently, our former findings indicated that an ideal CO_2 adsorbent is composed of a monolithic support with very high cell density and nonporous walls coated with an approximately 10 μm thick zeolite 13X film. The scope of the present work is to prepare such adsorbents and evaluate CO_2 separation performance by breakthrough experiments in combination with mathematical modelling.

2. Experimental section

2.1. Material synthesis and characterization

Steel monoliths with cylindrical-shape (from Metalit Emitec, Germany) with very high-density of 1600 cells per square inch (cpsi) were adopted as support for the fabrication of microchannel adsorbents. The outer steel shell of the monoliths is 15.2 cm in length and 3.0 cm in outer diameter, while the length of the honeycomb structure in the shell was 14.9 cm with a diameter of 2.8 cm, corresponding to a volume of 92 mL, see Fig. 1 a) and b). The surface area of the steel in these monoliths is 7332 cm^2 per monolith according to the supplier. The microchannels with a cross section of equilateral triangles with a width of 0.5 mm are shown in Fig. 1 c). The nonporous steel foil with thickness of 25 μm used to fabricate the monolith has a smooth surface, as shown in Fig. 1 c), d). Each steel monolith's weight was measured before start the seeding and film growing procedure.

Zeolite 13X films were grown on the monolith using a similar method as described before [29]. In brief, the monolith was first exposed to a 4% HF solution for 30 s. This step removed the surface coating on the stainless-steel casing and was found to be critical to avoid the formation of secondary phases, such as sodalite. Afterward, it was washed with a 0.1 M aqueous NH_3 solution and then soaked in a 0.4 wt% cationic polymer (type Redifloc 4150, from EKA Chemicals) solution in water at a pH value of 8 to make the steel surface charged positively. Zeolite FAU crystals with a particle size of 80 nm and octahedral shape was dispersed in DI water with concentration of 1 wt% and was adopted as seeding suspension. The seed crystals was prepared as described earlier [32,33], and briefly describe here. The composition of the synthetic solution in mol was 1 SiO_2: 0.29 Al_2O_3: 0.01 Na_2O: 0.72 $(TMA)_2O$: 118 H_2O. After mixing the chemicals, the mixture was hydrolysed for 24 h, and crystallization was performed at 100 °C under reflux for 120 h. The monolith was soaked in the seed suspension for about 1 h to form a monolayer of the FAU seeds on the positively charged surface. The excessive seeds as multilayer were cleared away by washing with a 0.1 M aqueous NH_3 solution. The monolayer of seed crystals is shown in Fig. 1(e) and (f). Afterwards, zeolite 13X films were grown inside the microchannel of the

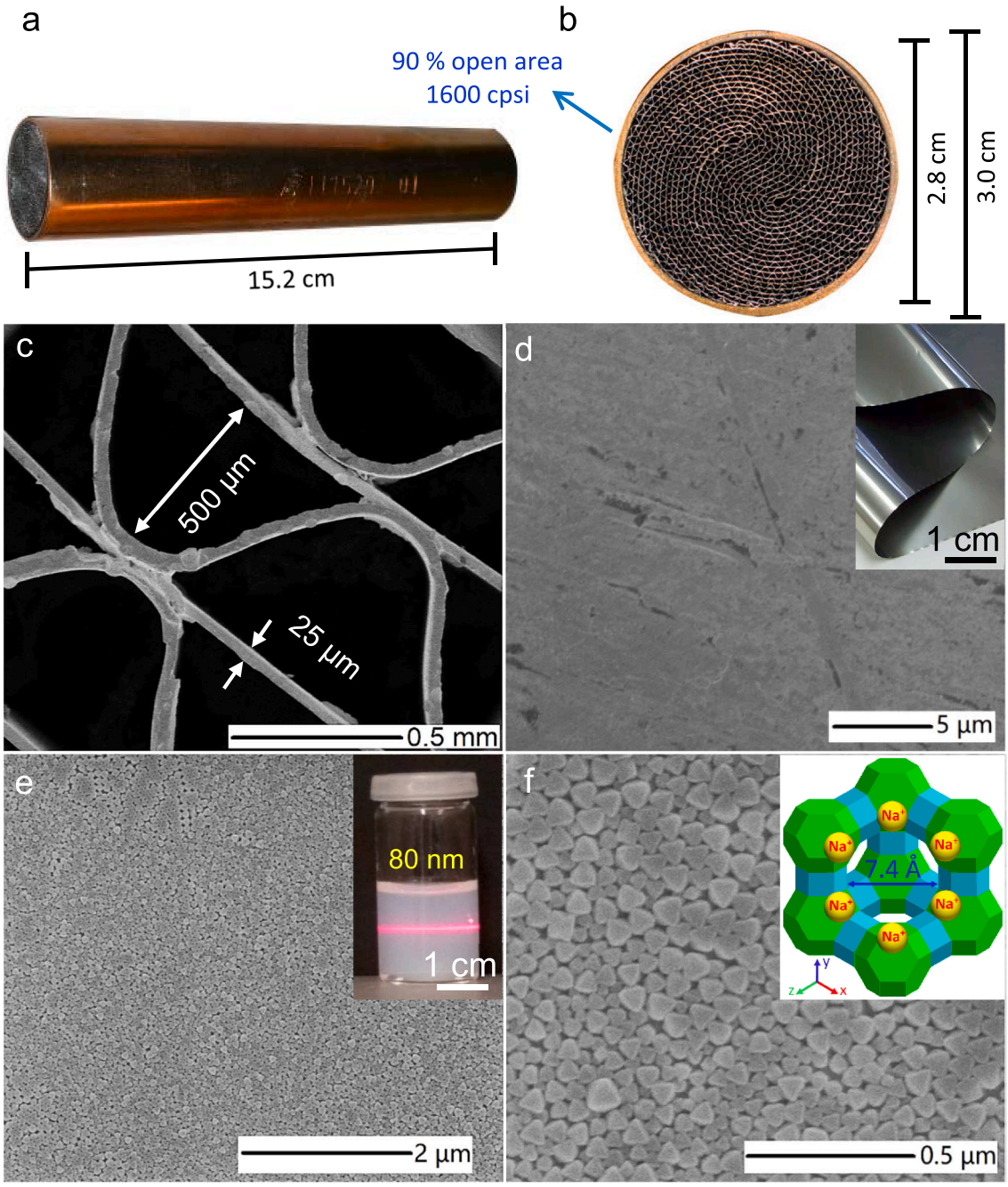

Fig. 1. Photographs of steel monoliths used as substrate material for the structured adsorbent (a) and (b), SEM images of cross view of monolith (c), the surface of bare steel foil (d), after coated with a monolayer of zeolite FAU seed (e) and (f). Insert in (d) is camera image of raw steel foil, insert in (e) is zeolite FAU colloid illuminated by a laser bar, insert in (f) is the structure of zeolite 13X framework, Na^+ cations are mainly located in the sodalite cage and hexagonal prism.

monoliths by repeated hydrothermal treatment in a transparent synthetic mixture with composition in mol of 1 SiO_2: 0.13 Al_2O_3: 9.13 Na_2O: 568 H_2O until the desired thickness was reached.

The monolith was raised and lowered repeatedly in the synthesis solution in order to remove air bubbles in the microchannels. The growth was conducted in a polymethylpentene (PMP) tube reactor, which was placed in a 90 °C oil bath and refluxed by a condenser. The films growth process was conducted in 21 steps of 65 min each to achieve a film thickness of about 3 µm, and 70 steps to reach film thickness of 11 µm. The sample was washed by a 0.1 M NH_3 solution after each step. And after the last step, the films coated monoliths were rinsed and dried at 120 °C in oven, then cooled in air before the weights of the samples were measured. The zeolite films' weights were calculated from the weight difference of the monolith after and before synthesis.

The pattern of the microchannel adsorbent was evaluated with the aid of field emission scanning electron microscope (SEM, Zeiss Merlin). Cross sections of the sorbent were produced by soaking the steel monolith into liquid nitrogen, after cool down quickly fracture it with a hammer. Energy dispersive spectroscopy (EDS, from Oxford Instruments, equipped with 50 mm^2 X-max detector,) was employed to determine the Si/Al and Na/Al ratios in the 13X films. The test was conducted at 10 kV at low magnification (100 times) utilizing a microinjector for the purpose of alleviate charging by gusting N_2 gas near the surface of the sorbents and thus avoiding the Na diffusion. The method was calibrated using a sample of zeolite A powder with known composition as a reference, as demonstrated elsewhere [34]. X-ray

diffraction (XRD) patterns were measured with a step size of 0.026° from 5° to 50° 2θ employing an X-ray diffractometer (Empyrean - Malvern Panalytical) provided with a PIXcel 3D detector and a Cu LFF HR X-ray tube.

2.2. Breakthrough experiments

Breakthrough assessments were conducted by utilizing four types of probing designs as shown in Fig. 2. Two steel monoliths were stacked up vertically in a steel column with 3.2 cm inner diameter for conducting breakthrough experiments. Graphite tapes (AESSEAL, Sweden) were wrapped around both ends of the monolith for preventing gas bypass through the void between column and monolith. Clean glass beads (3 mm) were loaded at the feed side (bottom) of the column, in order to decrease the entrance volume of the column. Before the measurement, the column temperature was increased to 150 °C and kept for 3 h, with a continuous flow of N_2 (Linde Gas, 99.99%) at a rate of 0.2 L/min. After cooling down, the CO_2 breakthrough assessments were measured at ambient pressure and room temperature. For this aim, a gas mixture composed of 10% CO_2 in N_2 (AGA Gas AB) with flow rate of 0.25, 0.50 or 1.00 L/min was employed as feed gas. The concentration of CO_2 from the effluent side of the column was detected by rapid response CO_2 infrared transducer (CA-10 CO_2 Analyzer with response time of 0.5 s, Sable Systems International). The adsorbent was regenerated by heating the column to 120 °C for several hours, with a N_2 flow of 0.2 L/min between each adsorption steps. During regeneration the heating rates were 2 °C/min, while the cooling rates were uncontrolled natural cooling.

2.3. Mathematical modelling of breakthrough data

The CO_2 adsorption capacity q for the 13X films in the microchannels of the monoliths was calculated based on the breakthrough result from the time t to arrive $C_{out}/C_0 = 0.5$ for 13X films grown monoliths and the time t to arrive $C_{out}/C_0 = 0.5$ for the bare monoliths using the equation as shown below:

$$q = \frac{p_{CO_2} F \left(t^{coated}_{C_{out}/C_0=0.5} - t^{uncoated}_{C_{out}/C_0=0.5} \right)}{RTm} \quad (1)$$

In this equation, R represents ideal gas constant, T means temperature of the gas, m stands for the mass of 13X films in the microchannels, p_{CO_2} indicates CO_2 partial pressure, and F represents the flow rate in the breakthrough measurement.

The breakthrough profiles were also modelled under the assumptions of an isothermal system with gas flow accounting for axial dispersion phenomena. The shape of the monolith channels was approximated as an equilateral triangle (parameters listed in Table 3). Adsorption was considered to occur in the zeolite film exclusively, due to the non-porous nature of the steel monolith walls. Moreover, for CO_2 breakthrough modelling the adsorption of the N_2 carrier could be considered practically negligible, being two orders of magnitude lower than the figure for the target adsorbate, as reported in the literature for zeolite 13X under operating conditions comparable to those investigated in this work [25].

The mass balance for CO_2 in a differential control volume of the structured adsorbent can be expressed as [35,36]:

Table 1
Film thickness, Si/Al and Na/Al ratios and zeolite mass for the adsorbents.

Growth steps	Thickness	Si/Al	Na/Al	Mass
21	3 μm	1.09	0.97	5.6 g
70	11 μm	1.10	0.98	19.8 g

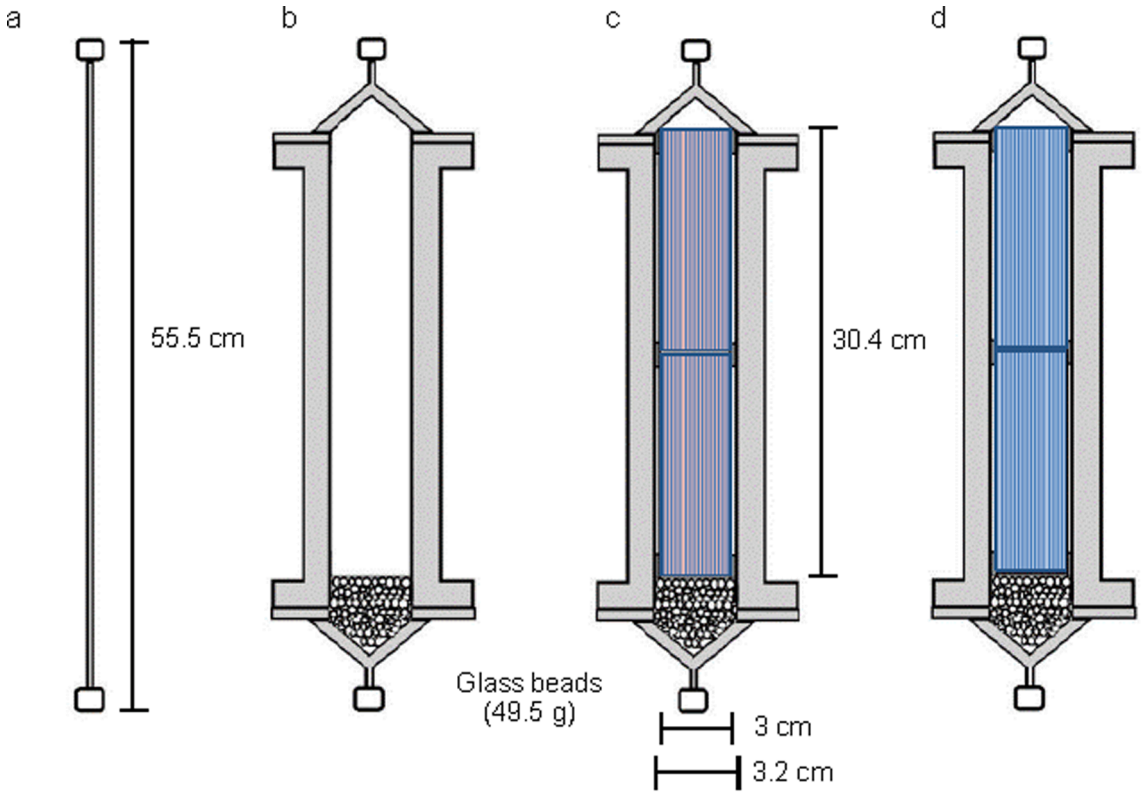

Fig. 2. Simplified diagrams of the various experimental designs assessed for breakthrough measurements: (a) steel pipe (1.5 mm) with 55.5 cm full length linked to the breakthrough equipment, (b) column (3.2 cm inner diameter) and glass beads, (c) column and glass beads inserted with two bare monoliths sealed by graphite tape, (d) column and glass beads inserted with two zeolite films coated monoliths sealed by graphite tape.

Table 2
Breakthrough data for 3 and 11 μm zeolite films at flowrates of 0.25, 0.50 and 1.00 L min^{-1}.

Monoliths	Time to reach $C_{out}/C_0 = 0.5$ (s) Gas flow rate [L min^{-1}]		
	0.25	0.50	1.00
Uncoated	52.7	25.2	13.0
3 μm film	876	445	238
11 μm film	3659	1639	723

$$-\varepsilon D_{ax}\frac{\partial^2 C}{\partial z^2} + \varepsilon\frac{\partial uC}{\partial z} + \varepsilon\frac{\partial C}{\partial t} + \rho_b\frac{\partial \overline{\omega}}{\partial t} = 0 \quad (2)$$

with the following initial and boundary conditions:

$$\overline{\omega}_{(t=0,z)} = 0 \quad (3)$$

$$C_{(t=0,z-\{0\})} = 0 \quad (4)$$

$$C_{(t,z=0)} = C_0 \quad (5)$$

$$\left.\frac{\partial C}{\partial z}\right|_{(t,z=L)} = 0 \quad (6)$$

The axial dispersion coefficient for laminar flow in the monolith channel can be computed as [37]:

$$D_{ax} = D_{CO_2\text{-}N_2} + \frac{u^2 d_h^2}{192 D_{CO_2\text{-}N_2}} \quad (7)$$

The rate of adsorption for the adsorbate was assumed to be governed by a linear driving force (LDF) [35]:

$$\frac{\partial \overline{\omega}}{\partial t} = k_{ov}(\omega^* - \overline{\omega}) \quad (8)$$

The thermodynamic adsorption equilibrium for the CO_2-zeolite system can be described by the Henry law [31]:

$$\omega^* = K_H P^* \quad (9)$$

The adoption of the Henry adsorption isotherm is justified by the practically linear trend of adsorption capacity vs. CO_2 partial pressure for a value of the latter smaller than 0.1 bar (the level adopted in this work for dynamic experiments), as retrieved in the literature for zeolite 13X at 25 °C [22].

The overall mass transfer resistance R_{ov} (equal to $1/k_{ov}$) of the adsorption process depends on the CO_2 diffusion in both the gas and zeolite films, with associated resistances termed R_{ext} and R_z, respectively. These transport mechanisms occur in series, and consequently R_{ov} can be expressed as [38]:

$$R_{ov} = R_{ext} + R_z \quad (10)$$

The gas film and zeolite layer diffusion resistances can be evaluated as [31,38]:

$$R_{ext} = \frac{d_h}{4k_{ext}} \quad (11)$$

$$R_z = \frac{\delta^2}{3D_z} \quad (12)$$

The gas film mass transfer coefficient k_{ext} was estimated *via* the following correlation proposed by Hawthorn for monoliths with channels with equilateral triangle-shape [39]:

$$Sh = 2.35\left(1 + 0.139 Re\ Sc\frac{d_h}{L}\right)^{0.81} \quad (13)$$

with Re = $\frac{d_h \rho_g u}{\text{Î¼}}$, $Sh = \frac{d_h k_{ext}}{D_{CO_2\text{-}N_2}}$ and Sc = $\frac{\text{Î¼}}{\rho_g D_{CO_2\text{-}N_2}}$.

The pressure drop across the structured adsorbents for laminar flow in equilateral triangular ducts can be calculated as [40]:

$$\frac{\partial P}{\partial z} = 26.66 \times 10^{-5}\frac{\mu u}{d_h^2} \quad (14)$$

The CO_2 adsorption capacity q^{model} was also estimated from the fitted model using the relation

$$q^{model} = \frac{\omega}{X_z} \quad (15)$$

The Aspen Plus Dynamics® simulation software package was adopted to solve mass and momentum balance equations (2), (8), (14) employing the method of lines. A Taylor-based Upwind Differencing Scheme was used to discretize first-order spatial derivatives and a second-order Central Differencing Scheme for the discretization of the second-order terms (axial dispersion in Eq. (2)). The overall mass transfer coefficient k_{ov} and the Henry equilibrium constant K_H were determined as best fitting parameters for the model, i.e., by minimizing the sum of squared differences between theoretical and experimentally determined values of CO_2 concentration at the adsorber outlet. The evaluation of the overall mass transfer resistance R_{ov} (through k_{ov}), and the estimation of R_{ext} (*via* Eqs. (11) and (13)) enables estimation of the zeolite film diffusion resistance R_z by means of Eq. (10). This in turn allows the determination of the kinetically controlling mass transfer mechanism for the process under analysis.

Table 3
Properties and main fluid dynamic/kinetic/thermodynamic parameters derived from the numerical model.

Parameters	3 μm film Gas flow rate [L min^{-1}]			11 μm film		
	0.25	0.50	1.00	0.25	0.50	1.00
L [m]	0.298					
D_{ax} [m^2 s^{-1}]	1.50×10^{-5}					
ε, [−]	0.89			0.84		
d_h [m]	5.26×10^{-4}			4.86×10^{-4}		
ρ_b [kg m^{-3}]	786			829		
x_z [kg kg^{-1}]	0.0388			0.1300		
R_{ext} [s]	1.96×10^{-3}			1.68×10^{-3}		
R_{ov} [s]	1.695	1.650	1.538	14.085	12.048	12.195
R_z [s]	1.693	1.648	1.536	14.083	12.046	12.193
D_z [m^2 s^{-1}]	1.77×10^{-12}	1.82×10^{-12}	1.95×10^{-12}	2.86×10^{-12}	3.35×10^{-12}	3.31×10^{-12}
ΔP [bar]	3.72×10^{-5}	7.44×10^{-5}	1.50×10^{-4}	4.62×10^{-5}	9.25×10^{-5}	1.85×10^{-4}
K_H [mol kg^{-1} bar^{-1}]	1.01	1.04	1.12	4.14	3.73	3.37
ω [mol kg^{-1}]	0.10	0.10	0.11	0.41	0.37	0.34
q^{model} [mol kg^{-1}]	2.6	2.6	2.9	3.2	2.8	2.6
q [mol kg^{-1}]	2.7	2.8	3.0	3.4	3.0	2.7

3. Results and discussion

3.1. Zeolite films

The zeolite films were grown from a highly uniform and close-packed monolayer of oriented FAU seed crystals, Fig. 1 e), f). As shown from the XRD pattern of the seed layer (Fig. 4), the crystals are highly (111)-oriented. The quality of the seed layer is important to produce zeolite film with uniform thickness [41–47] and the seed layer obtained in the present work seems ideal.

Fig. 3 demonstrates characteristic SEM images of the 13X films formed on steel wall in the microchannel adsorbents synthesized in this study. The top view images illustrate that the polycrystal on the film surface have standard FAU morphology and no other type zeolites with different morphologies, i.e., zeolite crystals of other phases are observed. Preliminary experiments showed that this multi-step synthesis was necessary to prevent the deposition of sediments and formation of hydroxy-sodalite crystals as observed in our earlier work [29] and arrive at uniform films. Also, the films are clean and free from any sediments of crystals deposited from the synthesis mixture as observed in earlier work [31]. Moreover, the prepared zeolite 13X film was continuous everywhere, has uniform thickness, and apparently be composed of well-

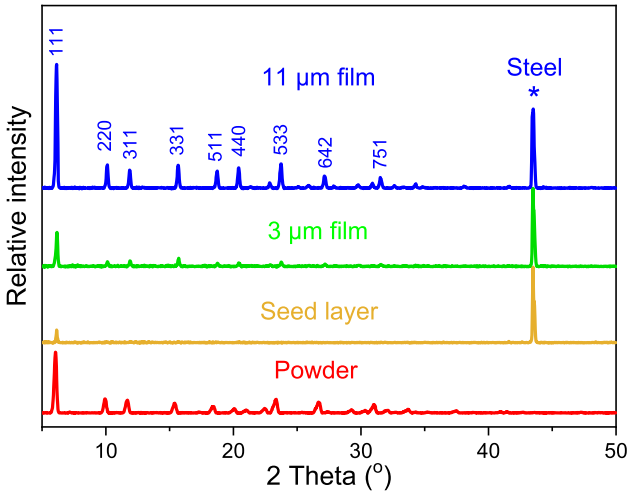

Fig. 4. XRD pattern of zeolite FAU seed powder, seed layer on steel foil, steel monolith coated with a 3 µm and 11 µm zeolite film. Reflections coming from steel substrate are marked by asterisk.

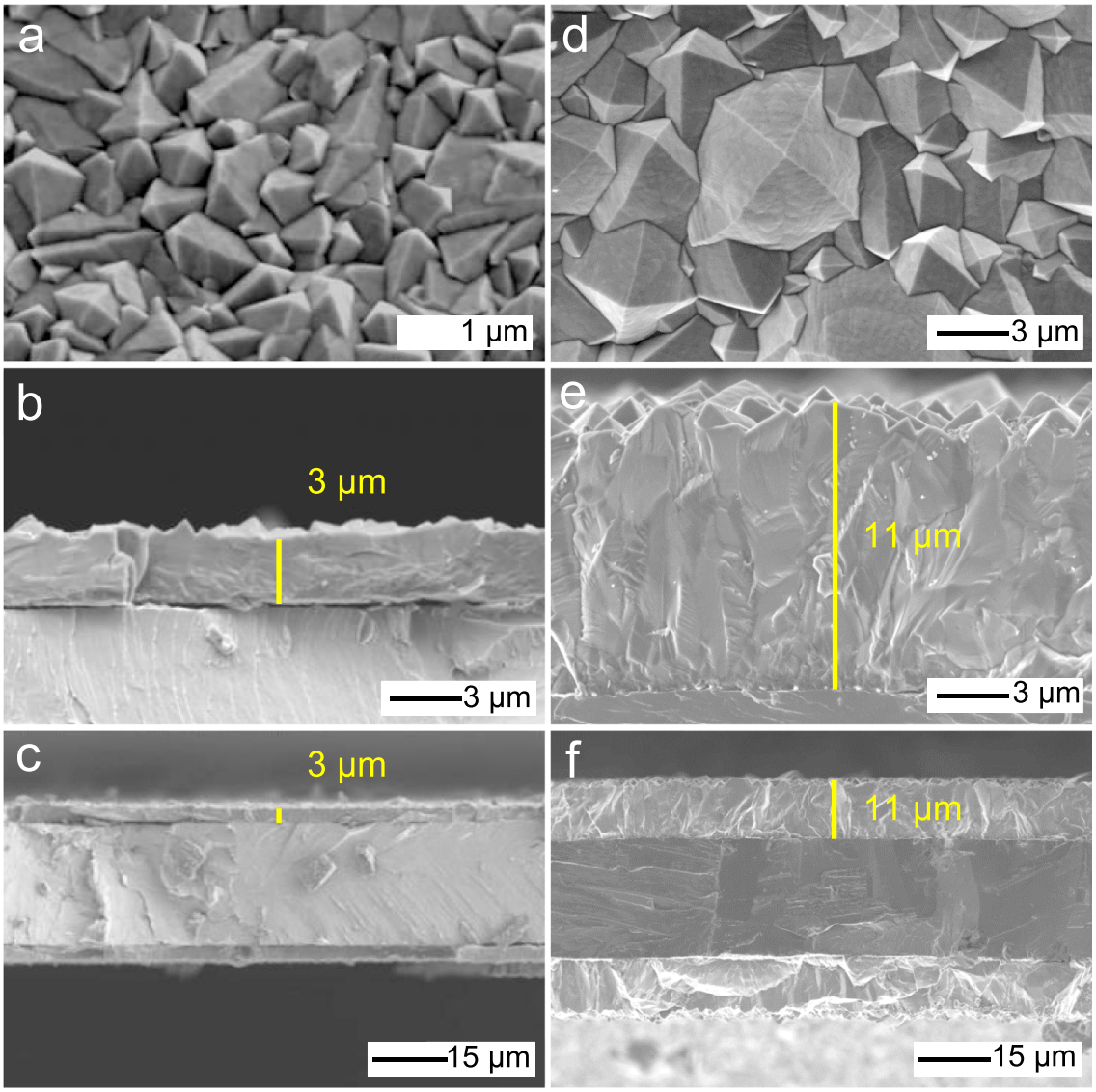

Fig. 3. SEM images of the microchannel adsorbent, 3 µm (left) and 11 µm films (right).

intergrown crystals, Fig. 3 a), b). The cross views in SEM images demonstrate that the walls of steel substrate were nonporous and quite smooth, which contrary to the cordierite-type monoliths used in our former study [31]. As illustrated in Fig. 3b) and e), the thickness of 13X film was approximately 3 μm for 21 steps synthesis, and 11 μm for 70 steps growth, as also shown in Table 1. Consequently, the film thickness increased with about 150 nm per step. For simplicity, the 13X films coated steel monoliths will be named as 3 μm film and 11 μm, respectively, film in the following discussion.

The EDS analysis results of the 3 μm and 11 μm films are shown in Table 1. The Si/Al molar ratio is within the scope of 1.09–1.10, and the Na/Al ratio is in the range of 0.97–0.98. This means the zeolite polycrystals in the films are Na form of FAU, i.e., zeolite 13X. The weights of the zeolite films, were 5.6 g and 19.8 g for the 3 μm and 11 μm films, respectively. The weight gain of the coating in the monolith channel is proportional to the film thickness, which in agreement with expectation.

Fig. 4 shows XRD data recorded for a powder of the 80 nm FAU seed crystals (red trace). The reflections are relatively broad with low intensity, due to the small crystal size [48]. The peak positions are typical for zeolite 13X ($Na_{88}[Si_{104}Al_{88}O_{384}]$) and all the observed diffraction peaks could be indexed as shown in Fig. 4. The relative peak intensities are typical for randomly oriented crystals, as evident by comparison with the ICDD reference pattern 01-070-2168 recorded for randomly oriented zeolite 13X crystals. Only (111) diffraction peak was observed from the 13X phase in the pattern for the monolayer of seed crystals on the coated steel foil (yellow trace). This shows that the crystals are preferentially (111)-oriented. The patterns for the 3 μm film (green trace) and 11 μm film (blue trace) show that the films comprise randomly oriented zeolite 13X crystals. In addition to those of typical zeolite 13X and steel substrate, no miscellaneous peaks were observed, which in agreement with EDS and SEM results.

3.2. CO_2 breakthrough experiments

Fig. 5 illustrates breakthrough result at a flow rate of 1.00 L/min measured for a steel pipe with inner diameter of 1.5 mm (as shown in Fig. 2a) attached to the breakthrough instrument. The narrow steel pipe has a small volume of about 4 mL, and a very short delay of only 0.2 s was noticed under this flow rate. As a result, this experiment tests the dispersion and response time generated by the breakthrough instruments and the CO_2 analyzer without an adsorbent column. The response time of the system is quite short, because CO_2 breakthrough

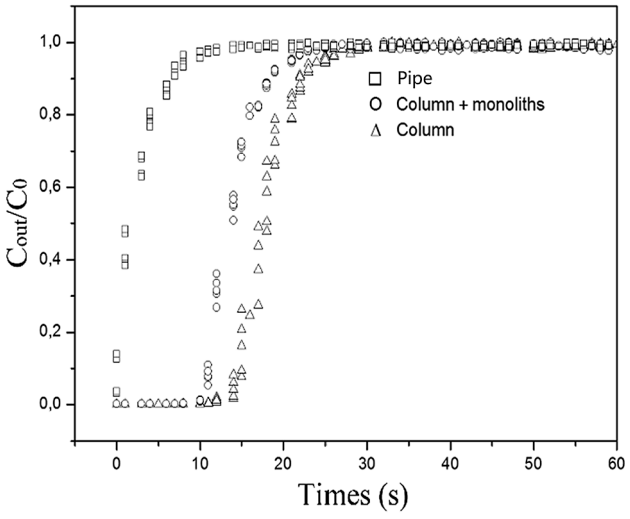

Fig. 5. Breakthrough results (squares, triangles, circles) at a flow rate of 1.00 L/min measured for steel pipe (ID 1.5 mm), column (ID 3.2 cm) and glass beads, column and glass beads inserted with two bare monoliths sealed by graphite tape as demonstrated in Fig. 2 a-c, respectively.

($C_{out}/C_0 > 0.05$) is detected within 1 s. The saturated CO_2 concentration of approximately 10% ($C_{out}/C_0 \approx 1$) is reached after 10 s, which corresponds to the dispersion time generated by the instruments without an adsorbent column.

The breakthrough result measured for the empty column with only glass beads (shown in Fig. 2b) linked to the breakthrough system at 1.00 L/min flow rate is illustrated also in Fig. 5. Because the void volume of the column with glass beads is 251 mL, that is remarkably higher than the 4 mL volume of steel pipe, the breakthrough front is shifted around 17 s, this time changing well match with the prospective postponement of 15 s as a result of gas filling in the bigger volume. Nevertheless, the distribution of the breakthrough front of the wide column is comparatively resemble to that of the narrow pipe, therefore the noticed distribution is just a consequence of distribution in the breakthrough instrument, it was not dispersion in the column.

Fig. 5 also reveals the breakthrough data measured when the column was inserted with two bare steel monoliths (as shown in Fig. 2c) at a flow rate of 1.00 L/min. Under this circumstance, the breakthrough front is moved 4 s in advance, which exactly in agreement with the prospective move because of the decreased volume of the column by inserting two non-porous-wall steel monoliths (4.5 s). Similarly, the distribution of the breakthrough front is approximately 10 s, owing to distribution in the breakthrough instrument without column. The time to attain $C_{out}/C_0 = 0.5$ for two bare monoliths is 13 s at flow rate of 1.00 L/min (mean value for five runs), as shown in Table 2.

Breakthrough result for the 3 μm thick 13X film coated steel monoliths are displayed in Fig. 6a). Overlapping and very sharp breakthrough curves were acquired after activation of the 13X films at 120 °C. Compared to the front measured for the column inserted with bare steel monoliths, the breakthrough front shows a little broadened. The times to arrive $C_{out}/C_0 = 0.5$ (average for 5 breakthrough experiments) for the different flow rates are shown in Table 2 and the corresponding CO_2 adsorption capacities q estimated directly from the breakthrough data using equation (1) are given in Table 3.

The adsorption capacity q in average for the 3 μm thick 13X film, measured using the 3 different flow rates, is 2.8 mol CO_2/kg zeolite. The estimated adsorption capacity varies a little for the three flow rates, but the normal deviation is as low as 0.1 mol CO_2/kg zeolite, that demonstrates the excellent accuracy of the breakthrough measurements.

Breakthrough result for the 11 μm thick 13X film coated steel monoliths are shown in Fig. 6 b). One more time, overlapping and sharp breakthrough curves with a little more broadened front (as a result of increased thickness of 13X coating) were received [49], while under this circumstance, the breakthrough of CO_2 appears significantly later as a result of the quite higher adsorption amount of the remarkably thicker 13X film. The times to reach $C_{out}/C_0 = 0.5$ for monoliths coated with 11 μm zeolite film are given in Table 2. It is very noteworthy that at the slowest flow rate of 0.25 L/min, the time to reach $C_{out}/C_0 = 0.5$ is as much as more than 1 h. The adsorption capacity q of CO_2 calculated by employing equation (1) are shown in Table 3. The mean value of adsorption capacity q is 3.0 mol CO_2/kg zeolite, i.e., slightly higher than that observed for the monoliths coated with a 3 μm zeolite film. While, under this condition, the result shows a little increased normal deviation of 0.3 mol CO_2/kg zeolite.

The average adsorption capacity for the 3 and the 11 μm monoliths estimated using equation (1) is 2.9 mol CO_2/kg 13X with a normal deviation of 0.2 mol CO_2/kg 13X. This value in the middle of the adsorption capacities of 2.5 and 3.6 formerly recorded by Rodrigues [22] and Myers [23], respectively, for zeolite 13X extrudates and powder. In addition, the highest observed adsorption capacity of 3.4 mol CO_2/kg zeolite is equal to 0.37 mmol CO_2/cm^3 adsorbent for the 11 μm monolith. This result is remarkably higher than the CO_2 capacity of 0.13 mmol/cm^3 for the 1200 cpsi cordierite monolith (with a surface area of 48.9 cm^2/cm^3) coated with 2.5 μm 13X film [31], which attribute to the higher cell density (with a larger surface area of 78.4 cm^2/cm^3) and thicker film loading in an equal unit volume of the final structure in this

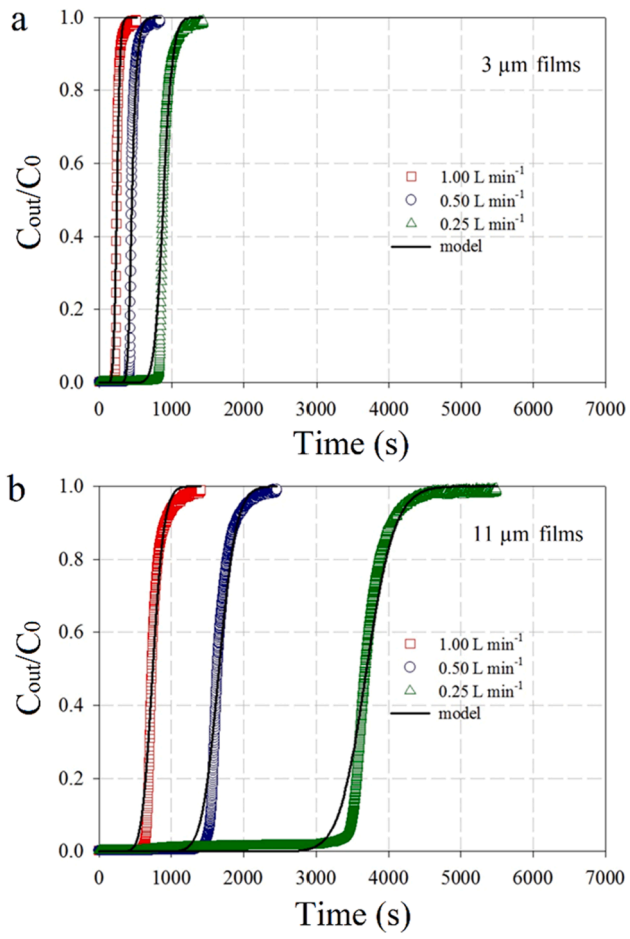

Fig. 6. Experimental (symbols) and model (lines) breakthrough curves for steel monolith coated with a 3 µm zeolite film a), and 11 µm zeolite film b) at different gas flow rates. Every breakthrough measurement is conducted 5 times and the 13X films are activated at 120 °C between the cycles.

work.

3.3. Modelling of the experimental data

Fig. 6 illustrates the model (curves) fitted to the experimental data (points) and Table 3 summarizes the main properties of these two structured adsorbents together with fluid dynamic/kinetic/thermodynamic parameters retrieved from the fitted model.

Fig. 6 shows that the adopted LDF-based model provides a satisfying interpretation of the CO_2 breakthrough data. Consequently, a good agreement between adsorption capacity q^{model} estimated from the fitted model using equation (15) and adsorption capacity q estimated using the simple equation (1) is observed, see Table 3. Secondly, the calculated values of D_{ax} highlight a practically negligible contribution of the axial dispersion to the overall dispersion of the breakthrough front as also indicated experimentally and discussed above. More specifically, D_{ax} coincide with the molecular diffusion coefficient $D_{CO_2\text{-}N_2}$, as derived from the application of Eq. (7). The computed pressure drops across the structured adsorbents were very low with ΔP falling in the range 10^{-5}–10^{-4} bar. As expected, ΔP linearly increases with the gas flow rate at fixed zeolite film thickness. Moreover, at fixed gas flow rate, the 11 µm zeolite film determined slightly greater values of ΔP due to both a greater gas velocity in the monolith channel (associated with a lower figure of the adsorbent void fraction) and a lower value of the hydraulic diameter d_h (cf. Table 3 and Eq. (14)). The very low ΔP displayed by the structured adsorbents would enable operation at very high flowrates and short cycle times. It is also fascinating to compare the mass transfer resistances in the systems. In fact, values of the mass transfer resistance in the gaseous film R_{ext} are 3 and 4 order of magnitude lower than the overall transport resistance R_{ov} for the 3 and 11 µm zeolite film, respectively. This clearly demonstrates that the transport of CO_2 in the zeolite layer represents the rate-determining step of the adsorption process, and it is $R_{ov} \approx R_z$. The Sherwood number calculated *via* Eq. (13) was 2.35 for all the analyzed cases, thus providing equivalent values for R_{ext} at fixed zeolite film thickness. In addition, the average value of R_z obtained for the thicker zeolite film is about 8 times greater than the average figure derived for the 3 µm zeolite film. This result is consistent with the dependence of R_z on the square of the zeolite layer thickness δ, as given in Eq. (12). However, the R_z values estimated for the thicker film are still low, which explains the sharp breakthrough fronts. In particular, the mass transfer coefficient figures estimated in this work are greater than common values reported in the literature for CO_2 adsorption onto zeolite beads/pellets [21,22]. For example, Yi et al. [50] derived an overall mass transfer coefficient k_{ov} of 0.035 s^{-1} from numerical analysis, adopting a linear driving force model, of CO_2 fixed bed adsorption tests performed at 323 K onto NaX zeolite pellets (particle size range 250–380 µm). The associated R_{ov} equals to 28.6 s, a figure that is 2.2 times greater than the average value retrieved in this work for the 11 µm film. Additionally, Sarker et al. [51] investigated CO_2 adsorption onto 1.68–2.38 mm zeolite 4A beads in a volumetric apparatus. The authors found a value of R_{ov} of about 1300 s ($k_{ov} = 7.7x10^{-4}$ s^{-1}) from a LDF model applied to the kinetic test performed at 293 K and 3.4 bar; this value is about two orders of magnitude higher than the one derived for the 11 µm zeolite film. Noteworthy, the estimated values of the zeolite film diffusivity – order of magnitude 10^{-12} m^2 s^{-1} – are in good agreement with those determined in the literature for CO_2 adsorption onto zeolite-coated cordierite monoliths and tested under comparable operating conditions [29–31]. It is once again remarked that both diffusion path and CO_2 intraparticle/zeolite film diffusivity significantly affect the overall mass transfer coefficient. Consequently, the deposition of a zeolite film of a few µm size can guarantee very low mass transfer limitations and very sharp breakthrough fronts.

It is highlighted that the adopted LDF model, even if was able to satisfactorily predict breakthrough curves, depends on a constant mass transfer coefficient not allowing to account for possible variations of zeolite film diffusivity along the adsorption process which could occur for strongly adsorbing systems with temperature variations. In this context, future numerical investigations should consider more rigorous diffusion-based model (such as the homogeneous surface diffusion model) also including diffusivity expressions depending on the surface coverage degree [52]. Moreover, in the present context an isothermal model was adopted since temperature variations in the fixed bed were practically negligible under the investigated operating conditions. In the light of adoption of continuous temperature swing adsorption systems, energy balance equations coupled with radial effects should be included in dynamic modelling due to the marked influence of temperature profiles on both adsorption and transport properties [53].

3.4. Comparison of physical properties with reported monoliths

Table 4 shows the physical properties of recently reported 3D-printed, extruded and cordierite-supported 13X monoliths. The performance of zeolite monolith can be improved by increasing the cell density [54]. In the current study, steel monoliths with very high cell density of 1600 cpsi were employed as substrates. This cpsi value is remarkably higher than 3D-print monoliths (with cpsi value in the range of 70–600) [12–16], extruded monoliths (cpsi value of 380 or 800) [18,19], cordierite monolith (cpsi value of 400 or 1200) [29,31] in former studies. Furthermore, high thermal conductivity is important to effectively conduct the heat released by the adsorption process [55]. The steel monolith supports used in the present work have a thermal conductivity of 50.2 W/mK, which provide faster heat conduction for the 13X films during adsorbent regeneration, where the thermal

Table 4
Properties and comparisons of zeolite 13X monoliths.

Monolith types	Cell density (cpsi)	Thermal conductivity (W/mK)	Mechanical strength (MPa)	Thickness (μm)	Capacity (mmol/g 13X)	Pressure drop ($\times 10^{-5}$ bar)	Ref
3D-print	380	0.1	0.69	650	1.8	n/a	12
3D-print	70	0.9	210	2200	2.0	n/a	14
3D-print	600	0.1	54.27	650	2.6	700	15
3D-print	160	0.1	n/a	800	n/a	n/a	16
3D-print	161	0.1	5.24	990	4.0	n/a	13
Extruded	380	0.1	n/a	900	2.1	n/a	18
Extruded	800	0.1	n/a	n/a	1.6	19,200	19
Cordierite	400	3	10	1.5	1.4	n/a	29
Cordierite	1200	3	25.5	2.5	3.0	n/a	31
Steel	1600	50.2[a]	1095[b]	11	3.4	4.6	This work

[a] Thermal conductivity of steel monolith support.
[b] Tensile strength of steel monolith support.

conductivity of pure zeolite 13X is only 0.08–0.13 W/m K [56]. The mechanical strength is important to allow straightforward handling of the material and stability during operation. The steel supports used in the present work offer excellent mechanical strength for the 13X films when compared with other types of self-supported monolithic adsorbents [57]. The adsorption capacity is another important property and it may be reduced using binder (inorganic, polymer) materials. The 11 μm film coated steel monolith has a dynamic adsorption capacity (3.4 mmol/g) that is higher than most reported structured sorbents and only second to the '3D-printed & soldered' zeolite 13X monolith (3.97 mmol/g) [13]. However, the latter adsorption capacity was measured at a higher CO_2 concentration (CO_2/N_2, 15/85 mixture) and a lower adsorption capacity would have been observed for a 10/90 mixture. Finally, low pressure drop is important in fast processes where high flow rates is necessary [58,59]. The adsorbents in the present work display a low pressure drop of only 4.6×10^{-5} bar at a high flow rate of 0.25 L/min. This is significantly lower than the reported pressure drops for 3D printed monolith of 7×10^{-3} bar [15], and for extruded monolith of 0.19 bar [19]. This extremely low ΔP would enable ultrafast CO_2 separation at very high flowrates and short cycle times.

4. Conclusion

In summary, we have developed a facile multistep synthesis strategy for fabricating zeolite 13X films with controlled thickness in microchannels of steel monolith. The structured adsorbents are calcination-free before use and showed excellent cyclic adsorption performance with the highest dynamic breakthrough capacity of 3.4 mol CO_2/kg zeolite. The 13X monolith has low energy cost for regeneration. The adsorbents displayed very sharp breakthrough fronts due to low mass transfer resistance in the 11 μm films. The steel monolith support endow 13X film high thermal conductivity that is an important characteristic required for rapid TSA applications; the ultra-low pressure drop greatly contribute to CO_2 separation with reduced energy costs; the high mechanical strength of the steel supports offer the 13X films better resistance to mechanical vibration and sustainability in harsh conditions. All these advantages make zeolite 13X coated steel monolith be a very promising alternative to traditional adsorbents in processes with short swing cycle times. We believe that the multistep synthesis strategy of present study will offer a novel route for designing and fabricating other types zeolite monoliths with optimal loadings, which open more other applications with improved performances like catalysis, membrane and sensor than CO_2 adsorption from flue gas.

CRediT authorship contribution statement

Jonas Hedlund: Conceptualization, Methodology, Funding acquisition, Supervision, Writing – review & editing. **Gustavo Garcia:** Validation, Investigation, Writing – original draft. **Marco Balsamo:** Methodology, Formal analysis. **Ming Zhou:** Investigation, Writing – original draft, Writing – review & editing. **Johanne Mouzon:** Resources, Supervision, Project administration.

Declaration of Competing Interest

The authors declare that they have no known competing financial interests or personal relationships that could have appeared to influence the work reported in this paper.

Acknowledgements

The Swedish International Development Cooperation Agency (SIDA), Ångpanneföreningens forskningsstiftelse (ÅForsk) and Bio4-Energy are gratefully acknowledged for financially supporting this work.

References

[1] G.T. Rochelle, Amine scrubbing for CO_2 capture, Science 325 (5948) (2009) 1652–1654.
[2] G. Yu, X. Zou, L. Sun, B. Liu, Z. Wang, P. Zhang, G. Zhu, Constructing connected paths between UiO-66 and PIM-1 to improve membrane CO_2 separation with crystal-like gas selectivity, Adv. Mater. 31 (2019) 1806853.
[3] M. Zhou, D. Korelskiy, P. Ye, M. Grahn, J. Hedlund, A uniformly oriented MFI membrane for improved CO_2 separation, Angew. Chem. Int. Ed. 53 (13) (2014) 3492–3495.
[4] L. Yu, A. Holmgren, M. Zhou, J. Hedlund, Highly permeable CHA membranes prepared by fluoride synthesis for efficient CO_2/CH_4 separation, J. Mater. Chem. A 6 (16) (2018) 6847–6853.
[5] S.J. Datta, C. Khumnoon, Z.H. Lee, W.K. Moon, S. Docao, T.H. Nguyen, I.C. Hwang, D. Moon, P. Oleynikov, O. Terasaki, K.B. Yoon, CO_2 capture from humid flue gases and humid atmosphere using a microporous coppersilicate, Science 350 (6258) (2015) 302–306.
[6] M. Zhou, S.G. Khokarale, M. Balsamo, J.P. Mikkola, J. Hedlund, Oligoamine ionic liquids supported on mesoporous microspheres for CO_2 separation with good sorption kinetics and low cost, J. CO_2 Util. 39 (2020), 101186.
[7] F. Akhtar, Q. Liu, N. Hedin, L. Bergström, Strong and binder free structured zeolite sorbents with very high CO_2-over-N_2 selectivities and high capacities to adsorb CO_2 rapidly, Energy Environ. Sci. 5 (6) (2012) 7664, https://doi.org/10.1039/c2ee21153j.
[8] M. Oschatz, M. Antonietti, A search for selectivity to enable CO_2 capture with porous adsorbents, Energy Environ. Sci. 11 (1) (2018) 57–70.
[9] W. Gao, S. Liang, R. Wang, Q. Jiang, Y. Zhang, Q. Zheng, B. Xie, C.Y. Toe, X. Zhu, J. Wang, L. Huang, Y. Gao, Z. Wang, C. Jo, Q. Wang, L. Wang, Y. Liu, B. Louis, J. Scott, A.C. Roger, R. Amal, H. He, S.E. Park, Industrial carbon dioxide capture and utilization: state of the art and future challenges, Chem. Soc. Rev. 49 (2020) 8584–8686.
[10] F. Su, C. Lu, CO_2 capture from gas stream by zeolite 13X using a dual-column temperature/vacuum swing adsorption, Energy Environ. Sci. 5 (10) (2012) 9021, https://doi.org/10.1039/c2ee22647b.
[11] F.J. Keil, Process intensification, Rev. Chem. Eng. 34 (2) (2018) 135–200.
[12] H. Thakkar, S. Eastman, A. Hajari, A.A. Rownaghi, J.C. Knox, F. Rezaei, 3D-printed zeolite monoliths for CO_2 removal from enclosed environments, ACS Appl. Mater. Interfaces 8 (41) (2016) 27753–27761.
[13] S. Wang, P. Bai, M. Sun, W. Liu, D. Li, W. Wu, W. Yan, J. Shang, J. Yu, Fabricating mechanically robust binder-free structured zeolites by 3D printing coupled with

zeolite soldering: a superior configuration for CO_2 capture, Adv. Sci. 6 (2019) 1901317.
[14] H. Thakkar, S. Lawson, A.A. Rownaghi, F. Rezaei, Development of 3D-printed polymer-zeolite composite monoliths for gas separation, Chem. Eng. J. 348 (2018) 109–116.
[15] S. Lawson, B. Adebayo, C. Robinson, Q. Al-Naddaf, A.A. Rownaghi, F. Rezaei, The effects of cell density and intrinsic porosity on structural properties and adsorption kinetics in 3D-Printed zeolite monoliths, Chem. Eng. Sci. 218 (2020), 115564.
[16] V. Middelkoop, K. Coenen, J. Schalck, M. Van Sint Annaland, F. Gallucci, 3D printed versus spherical adsorbents for gas sweetening, Chem. Eng. J. 357 (2019) 309–319.
[17] B. Verougstraete, A. Martín-Calvo, S.V. der Perre, G. Baron, V. Finsy, J.F. M. Denayer, A new honeycomb carbon monolith for CO_2 capture by rapid temperature swing adsorption using steam regeneration, Chem. Eng. J. 383 (2020), 123075.
[18] W.Y. Hong, S.P. Perera, A.D. Burrows, Comparison of MIL-101(Cr) metal-organic framework and 13X zeolite monoliths for CO_2 capture, Microporous Mesoporous Mater. 308 (2020), 110525.
[19] Q. Al-Naddaf, S. Lawson, A.A. Rownaghi, F. Rezaei, Analysis of dynamic CO_2 capture over 13X zeolite monoliths in the presence of SO_x, NO_x and humidity, AIChE J. 66 (2020), e16297.
[20] L.A. Darunte, Y. Terada, C.R. Murdock, K.S. Walton, D.S. Sholl, C.W. Jones, Monolith-Supported Amine-Functionalized Mg_2(dobpdc) Adsorbents for CO_2 Capture ACS Appl, Mater. Interfaces 9 (2017) 17042–17050.
[21] D.W. Breck, E.M. Flanigen, Molecular Sieves, Society of Chemical Industry, London, UK, 1968, pp. 47–60.
[22] S. Cavenati, C.A. Grande, A.E. Rodrigues, Adsorption equilibrium of methane, carbon dioxide, and nitrogen on zeolite 13X at high pressures, J. Chem. Eng. Data 49 (4) (2004) 1095–1101.
[23] J. A. Dunne, M. Rao, S. Sircar, R. J. Gorte, A. L. Myers, Calorimetric Heats of Adsorption and Adsorption Isotherms. 2. O2, N2, Ar, CO2, CH4, C2H6, and SF6 on NaX, H-ZSM-5, and Na-ZSM-5 Zeolites, Langmuir 12 (1996) 5896-5904.
[24] B. Besser, L. Häuser, L. Butzke, S. Kroll, K. Rezwan, Straightforward processing route for the fabrication of robust hierarchical zeolite structures, ACS Omega 2 (10) (2017) 6337–6348.
[25] P. Nugent, Y. Belmabkhout, S.D. Burd, A.J. Cairns, R. Luebke, K. Forrest, T. Pham, S. Ma, B. Space, L. Wojtas, M. Eddaoudi, M.J. Zaworotko, Porous materials with optimal adsorption thermodynamics and kinetics for CO_2 separation, Nature 495 (7439) (2013) 80–84.
[26] M.T. Ho, G.W. Allinson, D.E. Wiley, Reducing the cost of CO2 capture from flue gases using pressure swing adsorption, Ind. Eng. Chem. Res. 47 (14) (2008) 4883–4890.
[27] R.L. Siegelman, P.J. Milner, E.J. Kim, S.C. Weston, J.R. Long, Challenges and opportunities for adsorption-based CO_2 capture from natural gas combined cycle emissions, Energy Environ. Sci. 12 (7) (2019) 2161–2173.
[28] C. Kim, H.S. Cho, S. Chang, S.J. Cho, M. Choi, An ethylenediamine-grafted Y zeolite: a highly regenerable carbon dioxide adsorbent via temperature swing adsorption without urea formation, Energy Environ. Sci. 9 (2016) 1803–1811.
[29] A. Mosca, J. Hedlund, P.A. Webley, M. Grahn, F. Rezaei, Structured zeolite NaX coatings on ceramic cordierite monolith supports for PSA applications, Microporous Mesoporous Mater. 130 (1-3) (2010) 38–48.
[30] F. Rezaei, A. Mosca, P. Webley, J. Hedlund, P. Xiao, Comparison of traditional and structured adsorbents for CO_2 separation by vacuum-swing adsorption, Ind. Eng. Chem. Res. 49 (10) (2010) 4832–4841.
[31] F. Rezaei, A. Mosca, J. Hedlund, P.A. Webley, M. Grahn, J. Mouzon, The effect of wall porosity and zeolite film thickness on the dynamic behavior of adsorbents in the form of coated monoliths, Sep. Purif. Technol. 81 (2) (2011) 191–199.
[32] Q. Li, D. Creaser, J. Sterte, An investigation of the nucleation/crystallization kinetics of nanosized colloidal faujasite zeolites, Chem. Mater. 14 (3) (2002) 1319–1324.
[33] M. Zhou, M. Grahn, H. Zhou, A. Holmgren, J. Hedlund, The facile assembly of nanocrystals by optimizing humidity, Chem. Commun. 50 (91) (2014) 14261–14264.
[34] G. García, W. Aguilar-Mamani, I. Carabante, S. Cabrera, J. Hedlund, J. Mouzon, Preparation of zeolite A with excellent optical properties from clay, J. Alloys Compd. 619 (2015) 771–777.
[35] D.M. Ruthven, Principles of adsorption and adsorption processes, John Wiley & Sons, New York, 1984.
[36] F. Montagnaro, A. Silvestre-Albero, J. Silvestre-Albero, F. Rodríguez-Reinoso, A. Erto, A. Lancia, M. Balsamo, Post-combustion CO_2 adsorption on activated carbons with different textural properties, Microporous Mesoporous Mater. 209 (2015) 157–164.
[37] G.I. Taylor, Diffusion and mass transport in tubes, Proc. Phys. Soc. B 67 (1954) 857–869.
[38] F. Rezaei, P. Webley, Optimum structured adsorbents for gas separation processes, Chem. Eng. Sci. 64 (24) (2009) 5182–5191.
[39] R.D. Hawthorn, Afterburner catalysts-effects of heat and mass transfer between gas and catalyst surface (1974) 428-438.
[40] A.M. Holmgren, Enhanced mass transfer in monolith catalysts with bumps on the channel walls, Ind. Eng. Chem. Res. 38 (1999) 2091.
[41] A. Faisal, M. Zhou, J. Hedlund, M. Grahn, Recovery of butanol from model ABE fermentation broths using MFI adsorbent: a comparison between traditional beads and a structured adsorbent in the form of a film, Adsorption 22 (2016) 205–214.
[42] B. Zhang, M. Zhou, X. Liu, Monolayer assembly of oriented zeolite crystals on α-Al_2O_3 supported polymer thin films, Adv. Mater. 20 (11) (2008) 2183–2189.
[43] M. Zhou, X. Liu, B. Zhang, H. Zhu, Assembly of oriented zeolite monolayers and thin films on polymeric surfaces via hydrogen bonding, Langmuir 24 (20) (2008) 11942–11946.
[44] M. Zhou, J. Hedlund, Assembly of oriented iron oxide and zeolite crystals viabiopolymer films, J. Mater. Chem. 22 (47) (2012) 24877, https://doi.org/10.1039/c2jm35068h.
[45] M. Zhou, J. Hedlund, Oriented monolayers of submicron crystals by dynamic interfacial assembly, J. Mater. Chem. 22 (8) (2012) 3307, https://doi.org/10.1039/c2jm15990b.
[46] A. Farzaneh, M. Zhou, O.N. Antzutkin, Z. Bacsik, J. Hedlund, A. Holmgren, M. Grahn, Adsorption of butanol and water vapors in silicalite-1 films with a low defect density, Langmuir 32 (45) (2016) 11789–11798.
[47] A. Farzaneh, M. Zhou, E. Potapova, Z. Bacsik, L. Ohlin, A. Holmgren, J. Hedlund, M. Grahn, Adsorption of water and butanol in silicalite-1 film studied with in situ attenuated total reflectance-fourier transform infrared spectroscopy, Langmuir 31 (17) (2015) 4887–4894.
[48] M. Zhou, J. Hedlund, Facile preparation of hydrophobic colloidal MFI and CHA crystals and oriented ultrathin films, Angew. Chem. Int. Ed. 57 (34) (2018) 10966–10970.
[49] H. Ahn, S. Brandani, Analysis of breakthrough dynamics in rectangular channels of arbitrary aspect ratio, AIChE J. 51 (7) (2005) 1980–1990.
[50] H. Yi, H. Deng, X. Tang, Q. Yu, X. Zhou, H. Liu, Adsorption equilibrium and kinetics for SO_2, NO, CO_2 on zeolites FAU and LTA, J. Hazard. Mater. 203-204 (2012) 111–117.
[51] A.I. Sarker, A. Aroonwilas, A. Veawab, Equilibrium and kinetic behaviour of CO_2 adsorption onto zeolites, carbon molecular sieve and activated carbons, Energy Procedia 114 (2017) 2450–2459.
[52] V.J. Inglezakis, M.M. Fyrillas, J. Park, Variable diffusivity homogeneous surface diffusion model and analysis of merits and fallacies of simplified adsorption kinetics equations, J. Hazard. Mater. 367 (2019) 224–245.
[53] M.S. Shafeeyan, W.M.A. Wan Daud, A. Shamiri, Chem. Eng. Res. Des. 92 (2014) 961–988.
[54] A. Patton, B.D. Crittenden, S.P. Perera, Use of the linear driving force approximation to guide the design of monolithic adsorbents, Chem. Eng. Res. Des. 82 (8) (2004) 999–1009.
[55] L.W. Wang, Z. Tamainot-Telto, R. Thorpe, R.E. Critoph, S.J. Metcalf, R.Z. Wang, Study of thermal conductivity, permeability, and adsorption performance of consolidated composite activated carbon adsorbent for refrigeration, Renew. Energy. 36 (8) (2011) 2062–2066.
[56] K.C. Chan, C.Y.H. Chao, C.L. Wu, Measurement of properties and performance prediction of the new MWCNT-embedded zeolite 13X/$CaCl_2$ composite adsorbents, Int. J. Heat Mass Transf 89 (2015) 308–319.
[57] L. Baharudin, M.J. Watson, Monolithic substrate support catalyst design considerations for steam methane reforming operation, Rev. Chem. Eng. 34 (4) (2018) 481–501.
[58] B. Baghapour, M. Rouhani, A. Sharafian, S.B. Kalhori, M. Bahrami, A pressure drop study for packed bed adsorption thermal energy storage, Appl. Therm. Eng. 138 (2018) 731–739.
[59] M.H. Chahbani, D. Tondeur, Pressure drop in fixed-bed adsorbers, Chem. Eng. J. 81 (1-3) (2001) 23–34.